Article

Strain-Enhanced Thermoelectric Performance in GeS$_2$ Monolayer

Xinying Ruan [1,†], Rui Xiong [1,†], Zhou Cui [1], Cuilian Wen [1], Jiang-Jiang Ma [2,3], Bao-Tian Wang [2,3,4,*] and Baisheng Sa [1,*]

1 Key Laboratory of Eco-Materials Advanced Technology, College of Materials Science and Engineering, Fuzhou University, Fuzhou 350100, China; ruanxinyingjg@163.com (X.R.); rxiong421@163.com (R.X.); cuizhoufzu@163.com (Z.C.); clwen@fzu.edu.cn (C.W.)
2 Institute of High Energy Physics, Chinese Academy of Sciences (CAS), Beijing 100049, China; majj88@ihep.ac.cn
3 Spallation Neutron Source Science Center (SNSSC), Dongguan 523803, China
4 Collaborative Innovation Center of Extreme Optics, Shanxi University, Taiyuan 030006, China
* Correspondence: wangbt@ihep.ac.cn (B.-T.W.); bssa@fzu.edu.cn (B.S.)
† These authors contributed equally to this work.

Abstract: Strain engineering has attracted extensive attention as a valid method to tune the physical and chemical properties of two-dimensional (2D) materials. Here, based on first-principles calculations and by solving the semi-classical Boltzmann transport equation, we reveal that the tensile strain can efficiently enhance the thermoelectric properties of the GeS$_2$ monolayer. It is highlighted that the GeS$_2$ monolayer has a suitable band gap of 1.50 eV to overcome the bipolar conduction effects in materials and can even maintain high stability under a 6% tensile strain. Interestingly, the band degeneracy in the GeS$_2$ monolayer can be effectually regulated through strain, thus improving the power factor. Moreover, the lattice thermal conductivity can be reduced from 3.89 to 0.48 W/mK at room temperature under 6% strain. More importantly, the optimal ZT value for the GeS$_2$ monolayer under 6% strain can reach 0.74 at room temperature and 0.92 at 700 K, which is twice its strain-free form. Our findings provide an exciting insight into regulating the thermoelectric performance of the GeS$_2$ monolayer by strain engineering.

Keywords: GeS$_2$ monolayer; strain engineering; first-principles calculations; thermoelectric materials; thermal conductivity

1. Introduction

Thermoelectric technology is one of the most fantastic energy-conversion technologies that can convert heat energy and electrical energy into each other directly [1–3]. Thermoelectric materials have recently gained extensive attention as a critical factor for thermoelectric technology. The figure of merit ZT can be directly used to visualize the thermoelectric conversion efficiency of thermoelectric materials and can be calculated by [4–7]:

$$ZT = \frac{S^2 \sigma T}{\kappa} \tag{1}$$

where S stands for the Seebeck coefficient, σ is electrical conductivity, and T represents temperature. κ is the thermal conductivity, consisting of both electronic and lattice parts. Herein, the thermoelectric power factor (PF) can be defined as PF = $S^2\sigma$. Apparently, a higher PF and lower κ can contribute to an immense ZT value.

The development of 2D materials provides an excellent platform for discovering novel high-performance thermoelectric materials [8–13]. Previous studies have reported graphene [14,15], phosphorene (BP) [16–18], IVA–VIA compounds [19–21], and transition metal dichalcogenides (TMDs) [22–24], and all show excellent thermoelectric performance. In particular, IVA–VIA compounds exhibit high ZT values due to their ultralow lattice

thermal conductivities [19,20]. Recently, the 1T-GeS$_2$ monolayer has been reported as a potential thermoelectric material due to its relatively high electronic fitness function (EFF) value from high-through computational screening [21]. Moreover, the high-power factor of the GeS$_2$ monolayer further reveals its great potential application in the field of thermoelectrics [25]. However, the ZT value of the 1T-GeS$_2$ monolayer is only 0.23 when the thermal transport property is considered [25], which significantly hinders its further application. Therefore, it is of great significance to improve its thermoelectric performance by adjusting the thermal transport properties of GeS$_2$ monolayers. It is worth mentioning that the electronic structures of 2D materials are easily affected by applied strains [26–28]. Strain engineering has been theoretically and experimentally proposed as a valid way to enhance the thermoelectric properties of 2D thermoelectric materials [29,30]. Experimentally, the thermal conductivity of the Bi$_2$Te$_3$ monolayer can be reduced by 50% by applying a tensile strain of 6% [31]. Theoretically, tensile strain can significantly enhance Seebeck coefficients while reducing thermal conductivity, and this has been observed in the PtSe$_2$ monolayer [32]. Therefore, it is very interesting to investigate the strain effect on the electronic and thermoelectric properties of the GeS$_2$ monolayer.

In the present work, based on first-principles calculations and by solving the semi-classical Boltzmann transport equation, we systematically studied the tensile strain effects on the thermoelectric properties of the GeS$_2$ monolayer, including electronic structures, electronic transport properties, and phonon transport properties. It was found that the valence band near the Fermi level of the GeS$_2$ monolayer will degenerate under tensile strain, which leads to an improvement in the power factor. Meanwhile, the phonon group velocities and phonon relaxation times decrease with an increasing tensile strain, resulting in a reduction in the lattice thermal conductivity, thereby enhancing the thermoelectric performance. Our results provided a new tactic for improving the thermoelectric properties of the GeS$_2$ monolayer.

2. Methods

Our simulation works were based on first-principles calculations with the projector augmented-wave (PAW) [33] method, which is executed by the VASP [34] code, and the corresponding results were dealt with the ALKEMIE platform [35]. The generalized gradient approximation [36] with the Perdew–Burke–Ernzerhof functional (GGA-PBE) [37] was used to deal with the interaction between electronics and ions. The structure of the GeS$_2$ monolayer was completely optimized until the energy and force convergence criteria were less than 10^{-6} eV and -0.01 eV, respectively. The cutoff energy was set to 600 eV, and a k-point mesh of $15 \times 15 \times 1$ was adopted [38]. A vacuum thickness of 20 Å perpendicular to the in-plane direction of the GeS$_2$ monolayer was built. The Heyd–Scuseria–Ernzerhof (HSE06) [39] hybrid functional with a range-separation parameter of 0.2 and mixing parameter of 0.25 was also adopted to obtain more accurate band structures and electronic transport properties of the GeS$_2$ monolayer. The ab initio molecular dynamics (AIMD) simulations with the Nosé –Hoover thermostat (NVT) ensemble and a time step of 2ps were performed to investigate the thermal stability of the GeS$_2$ monolayer [40,41].

A denser k-point mesh of $35 \times 35 \times 1$ was used for static calculations to obtain more accurate electronic structures to solve semi-classical Boltzmann transport equations, which is realized in the BoltzTraP code [42]. The phonon spectrum and second-order anharmonic force constants were calculated by the Phonopy package [43] with a $6 \times 6 \times 1$ supercell, while a $4 \times 4 \times 1$ supercell was used to calculate third-order interatomic force constants. The sixth nearest neighbors were selected to obtain the third-order interatomic force constants to ensure the accuracy of lattice thermal conductivity and save the calculation time. Combing with second-order anharmonic force constants and third-order interatomic force constants as input files, the lattice thermal conductivity of the GeS$_2$ monolayer can be obtained through the ShengBTE code [44].

3. Results and Discussion

3.1. Structural Stability and Band Structure

Similar to the 1T-MoS$_2$ monolayer [45], each unit cell of the GeS$_2$ monolayer consists of one Ge atom and two S atoms with the Ge sublayer sandwiched between two S sublayers. The side and top views of the GeS$_2$ monolayer are plotted in Figure 1a,b, respectively. The relaxed lattice parameters are $a = b = 3.44$ Å, which agree with previous theoretical predictions [21,25]. Figure 1c describes the atom orbitals project band structure of the GeS$_2$ monolayer. It is clear that the GeS$_2$ monolayer demonstrates indirect band gap semiconductor features with a band gap of 1.50 eV. It is noted that the relatively large band gap can effectively prevent the bipolar conduction behavior in the materials and thus prevents the thermoelectric performance from being destroyed. Moreover, the VBM is mainly contributed by the S-p orbital, while the CBM is occupied by both Ge-s and S-p orbitals. Our results are in accordance with the previous theoretical predicated [25,46], indicating that our calculation parameters are reasonable.
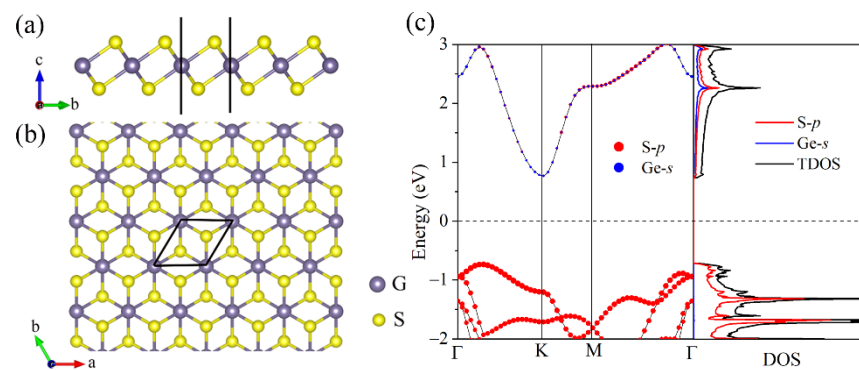

Figure 1. The structure of GeS$_2$ monolayer's (**a**) side and (**b**) top views. (**c**) The atom orbitals' project band structure and DOS for GeS$_2$ monolayer.

To understand the stability of the GeS$_2$ monolayer, we then conducted phonon spectrum calculations and AIMD simulations to explore the lattice and thermal dynamic stabilities, respectively. Figure 2a describes the phonon spectrum for the GeS$_2$ monolayer. Obviously, there are nine dispersion curves with three acoustic branches and six optical branches since a GeS$_2$ unit cell contains three atoms. Moreover, no imaginary frequency can be found in phonon dispersion curves, indicating that the GeS$_2$ monolayer possesses a good lattice dynamic stability. It is noted that the ZA mode for the GeS$_2$ monolayer near the Γ point is quadratically converged, which can be usually observed in 2D materials systems [47]. Furthermore, from the PhDOS of the GeS$_2$ monolayer, we know that the low- and high-frequency regions are mainly contributed by Ge and S atoms, respectively. Moreover, the phonon spectrum of the GeS$_2$ monolayer under 2% compressive strain was also calculated, as shown in Figure S1. A negative frequency was observed in the phonon spectrum, indicating the instability of the GeS$_2$ monolayer under compressive strain. Hence, in our study, we mainly concentrated on the tensile strain effects on the thermoelectric properties of the GeS$_2$ monolayer. Figure 2b illustrates the energy evolution and structure snapshot of the GeS$_2$ monolayer for 10 ps at 300 K. It is clear that the changes in total energy are minimal, and atoms are slightly vibrating around their equilibrium positions, suggesting that the GeS$_2$ monolayer exhibits excellent thermal dynamic stability as well.

Figure 3 illustrates the band structures of the GeS$_2$ monolayer at different biaxial tensile strains. Herein, the tensile strains can be calculated by $\varepsilon = (a - a_0)/a_0 \times 100\%$, where a_0 stands for the lattice constant when unstrained, while a represents the lattice constant under strain. Obviously, within our investigated strain range (0~6%), the band gap of the GeS$_2$ monolayer increases gradually with tensile strain since CBM moves toward the higher energy level. Additionally, with the increases in tensile strain, the valence bands between K and Γ points move toward the Fermi level, which can enhance the degeneracy

of the valence band and thus improve the Seebeck coefficient. Moreover, the band structure of the GeS$_2$ monolayer under 8% tensile strain was also calculated, as shown in Figure S2. However, the valence band maximum shifts to the position between Γ and K under 8% tensile strain. This phenomenon will decrease band degeneracy in the GeS$_2$ monolayer, which is not conducive to the thermoelectric application. Hence, in our study, we mainly concentrate on the 2–6% tensile strain effects on the thermoelectric properties of the GeS$_2$ monolayer. These consequences indicate that the tensile strain can effectively regulate the electronic structures of the GeS$_2$ monolayer. Therefore, an improvement in thermoelectric performance in the GeS$_2$ monolayer is anticipated [48,49].
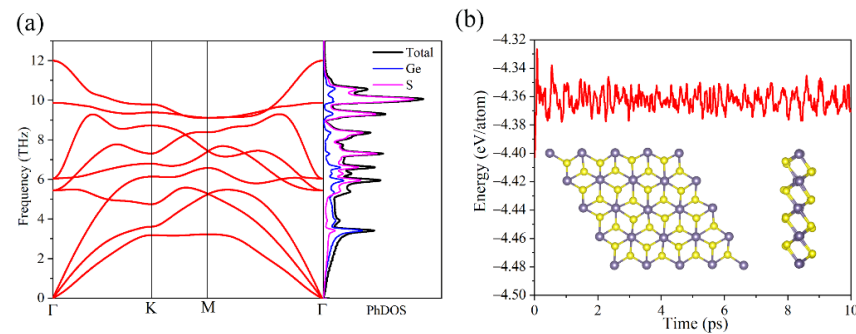

Figure 2. The (**a**) phonon spectrum and PhDOS of GeS$_2$ monolayer and (**b**) total energies evolution and structure snapshots after 10 ps AIMD simulations at 300 K for GeS$_2$ monolayer.
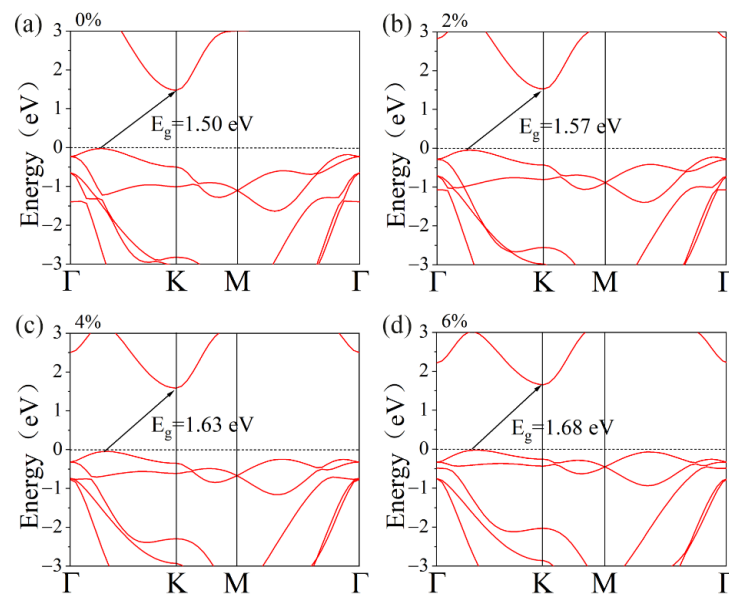

Figure 3. Band structures under different biaxial tensile strains of(**a**) 0%, (**b**) 2%, (**c**) 4% and (**d**) 6% for GeS$_2$ monolayer.

3.2. Electronic Transport Properties

We next investigate the effect of biaxial tensile strains on the electronic transport properties of the GeS$_2$ monolayer, including the Seebeck coefficient (S), electric conductivity (σ), electronic thermal conductivity (κ_e), and the power factor (PF). Figure 4 shows the contour maps of the Seebeck coefficient with respect to chemical potential under different biaxial tensile strains. Clearly, the S increases with an increasing tensile strain and decreases with an increasing temperature. The maximum S increases from 2386 μVK^{-1} (2318 μVK^{-1}) to 2697 μVK^{-1} (2605 μVK^{-1}) under p-type (n-type) doping, as the tensile strain augments from 0 to 6%. This phenomenon is mainly contributed by enlarging the band gap and band degeneracy in the GeS$_2$ monolayer with the increase in tensile strain.
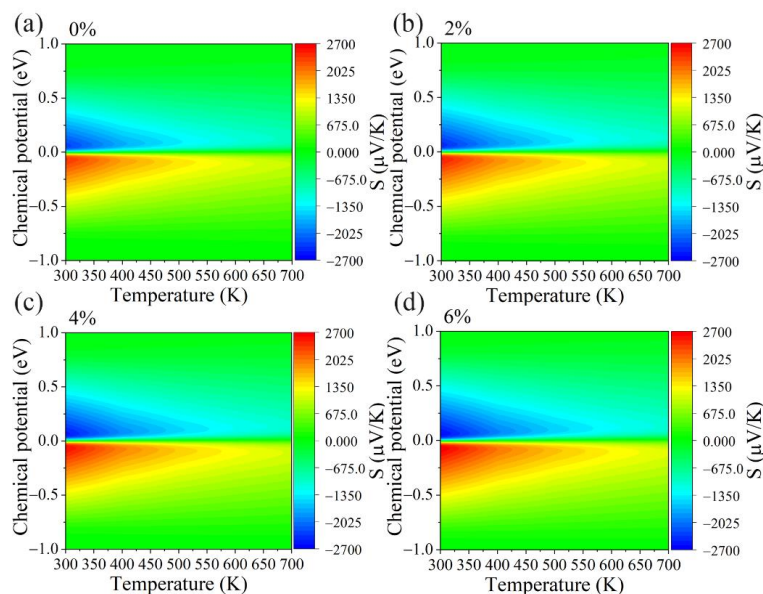
Figure 4. The contour maps of the Seebeck coefficient *S* with respect to chemical potential under different biaxial tensile strains of (**a**) 0%, (**b**) 2%, (**c**) 4% and (**d**) 6% for GeS$_2$ monolayer.

On the other hand, Figure 5a–d shows the electrical conductivity divided by the relaxation time (σ/τ) of the GeS$_2$ monolayer under different tensile strains. Contrary to the Seebeck coefficients, electrical conductivity is insensitive to the temperature and decreases with an increasing tensile strain. A similar tendency as σ/τ can be observed in electronic thermal conductivity (Figure 6a–d) since it can be calculated by [50]: $\kappa_e = L\sigma T$, where L represents the Lorenz number. Our results above show that the *S* and σ/τ exhibit opposite trends under tensile strain. Hence, we also calculated the power factor (PF) under different tensile strains, and the corresponding results are shown in Figure 7a–d. Apparently, the optimal value of the PF under p-type doping is much higher than n-type doping for all cases. More importantly, the PF gradually increases as the tensile strain is applied, which is due to the fact that the applied tensile strain has a more significant effect on the *S* than the σ/τ. The power factor as a function of carrier concentrations is also plotted in Figure S3.
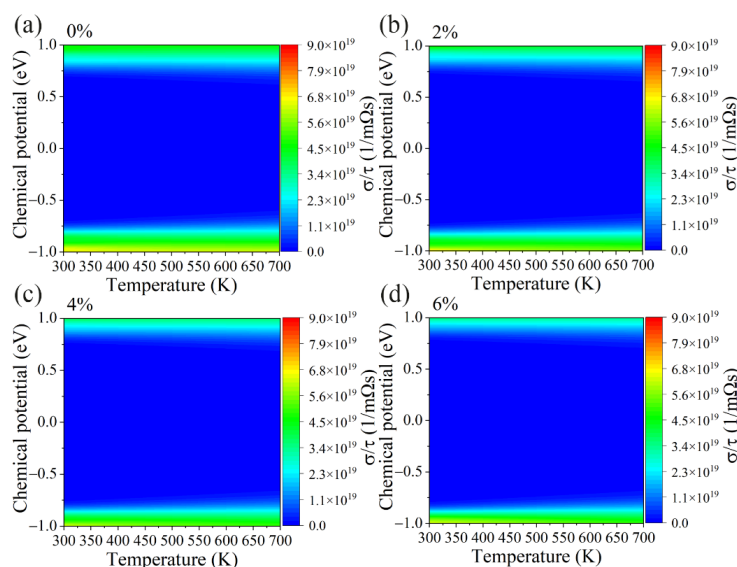

Figure 5. The contour map of the electrical conductivity divided by relaxation time (σ/τ) with respect to chemical potential under different biaxial tensile strains of (**a**) 0%, (**b**) 2%, (**c**) 4% and (**d**) 6% for GeS$_2$ monolayer.
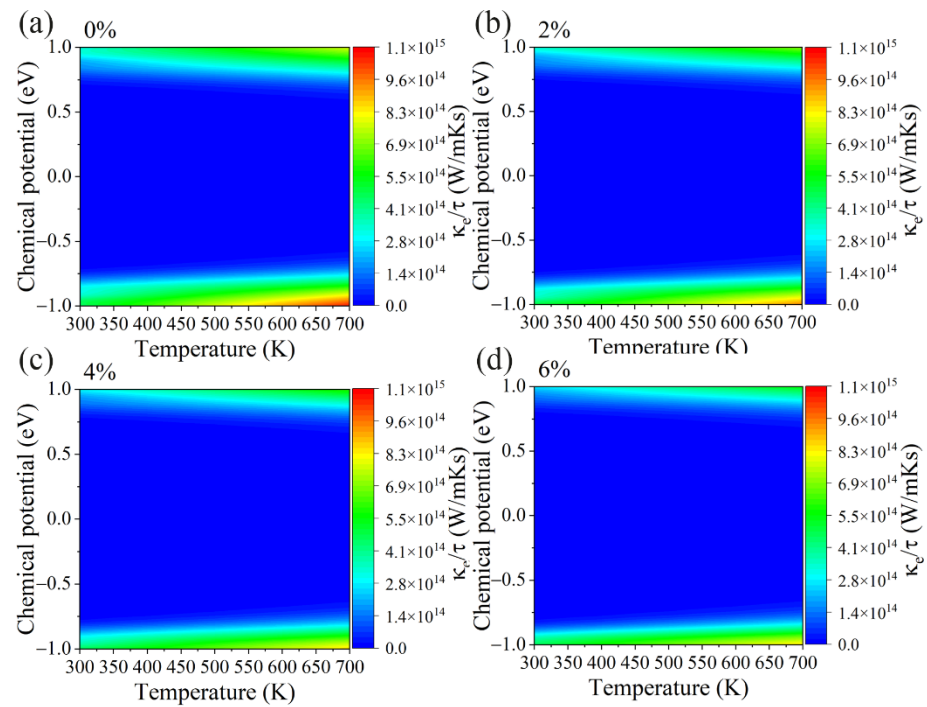
Figure 6. The contour map of the electronic thermal conductivity divided by relaxation time (κ_e/τ) with respect to chemical potential under different biaxial tensile strains of (**a**) 0%, (**b**) 2%, (**c**) 4% and (**d**) 6% for GeS$_2$ monolayer.
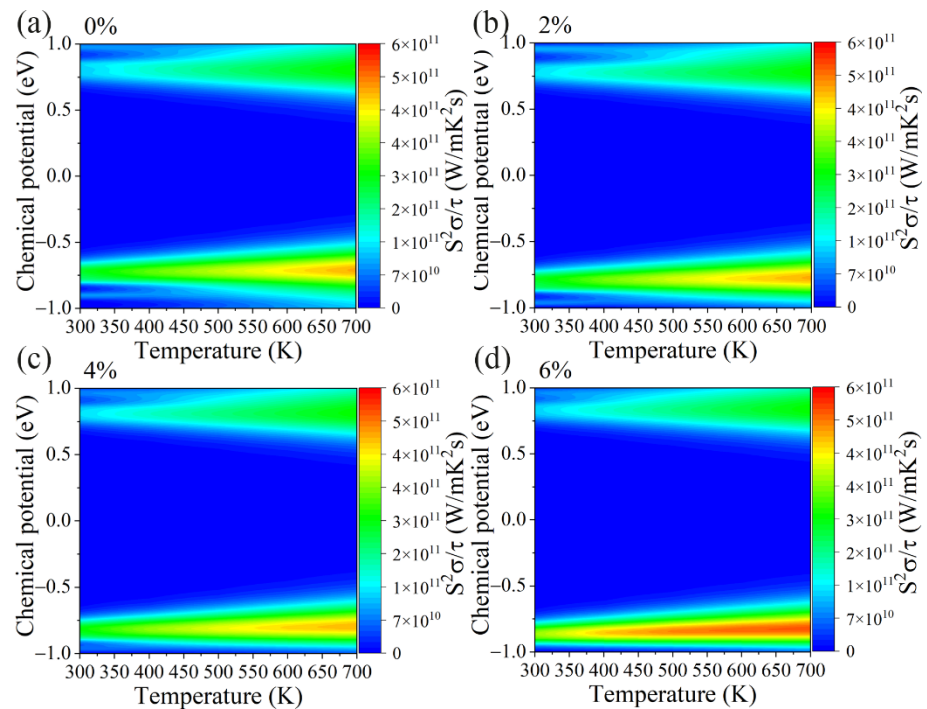

Figure 7. The contour map of the power factor divided by relaxation time ($S^2\sigma/\tau$) with respect to chemical potential under different biaxial tensile strains of (**a**) 0%, (**b**) 2%, (**c**) 4% and (**d**) 6% for GeS$_2$ monolayer.

3.3. Phonon Dispersion Curves and Transport Properties

Phonon thermal transport property is another critical factor for thermoelectric materials. Hence, the effect of tensile strain on the phonon transport properties of the GeS$_2$ monolayer was investigated in the following. The phonon dispersion curves under differ-

ent strains are illustrated in Figure 8. Clearly, no negative frequency was observed in any of the cases, suggesting that the GeS$_2$ monolayer's lattice is dynamically stable under these tensile strains. Furthermore, the frequencies of both optical and acoustic phonon modes gradually decrease with the increase in the tensile strain, leading to reducing phonon group velocities and thus a lower lattice thermal conductivity. This phenomenon is beneficial for the application of GeS$_2$ monolayer in the fields of thermoelectrics.
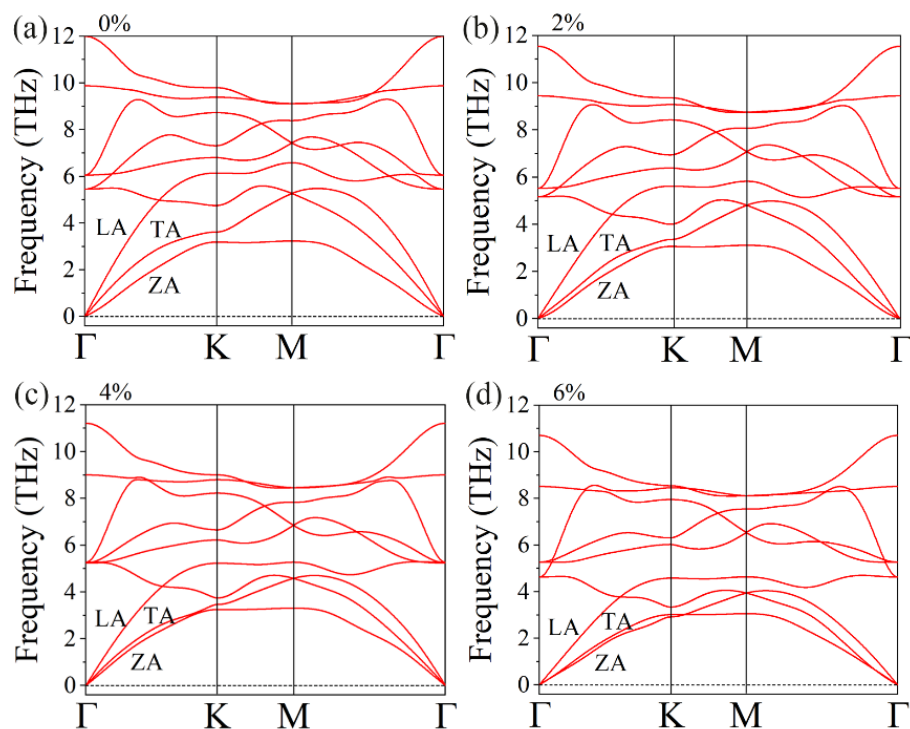
Figure 8. The phonon spectrum of GeS$_2$ monolayer under different biaxial tensile strains of (**a**) 0%, (**b**) 2%, (**c**) 4% and (**d**) 6%.

To evaluate the convergence of the lattice's thermal conductivity, we calculated the lattice thermal conductivity as a function of the nearest neighbor atomic, which is plotted in Figure S4. It is noted that the lattice thermal conductivity can reach good convergence criteria when the nearest neighbor atom is up to six. Figure 9a describes the lattice thermal conductivity (κ_1) of the GeS$_2$ monolayer with respect to temperature under different tensile strains. It is interesting to note that κ_1 decreases with both increasing temperature and tensile strain. For example, the κ_1 of the unstrained GeS$_2$ monolayer reduces from 3.89 to 1.13 W/mK when the temperature increases from 300 K to 1000 K. More importantly, the κ_1 will reduce to 0.48 W/mK when 6% strain is applied at 300 K. Such a small κ_1 is comparable to some recently reported novel 2D thermoelectric materials, such as a SnTe monolayer (0.67 W m^{-1} K^{-1}) [51], Sb$_2$Te$_2$Se monolayer (0.46 W m^{-1} K^{-1}) [52], and HfSe$_2$ monolayer (0.7 W m^{-1} K^{-1}) [53]. To unravel the strain-induced reduced lattice thermal conductivity behavior in the GeS$_2$ monolayer, we also calculated the phonon group velocities (v_λ) and phonon relaxation times (τ_λ) since κ_1 can be obtained by [54]:

$$\kappa_1 = \frac{\sum_\lambda C_\lambda v_\lambda^2 \tau_\lambda}{V} \tag{2}$$

where V represents the volume, which can be defined as $V = Sh$, where S is the cross-sectional area and h is the layer thickness of the GeS$_2$ monolayer. The layer thickness is obtained by the distance between the top and bottom surface atoms plus the Van der Waals radii of the surface atoms. C_λ is capacity heat. At room temperature, the capacity heat follows the Dulong–Petit limit; thus, κ_1 is mainly contributed by v_λ and τ_λ. Figure 9b,c show

v_λ and τ_λ of the GeS$_2$ monolayer under different tensile strains, respectively. Both v_λ and τ_λ decrease with an increasing tensile strain. This phenomenon leads to a decrease in the κ_l with an increasing tensile strain, which agrees with our previous results. Moreover, the calculated average value of v_λ is reduced from 1.14 to 1.08 Km/s, while the average value of τ_λ decreases from 0.94 to 0.25 ps when the strain rises from 0 to 6%. Such small v_λ and τ_λ further guarantee the low κ_l of the GeS$_2$ monolayer. Furthermore, we also calculated the Grüneisen parameters of the GeS$_2$ monolayer, as shown in Figure 9d. Interestingly, when the strain rises to 6%, the average value of Grüneisen parameters is enhanced from 1.11 to 3.15, indicating that anharmonic phonon interaction of the GeS$_2$ monolayer is strengthened under tensile strain.
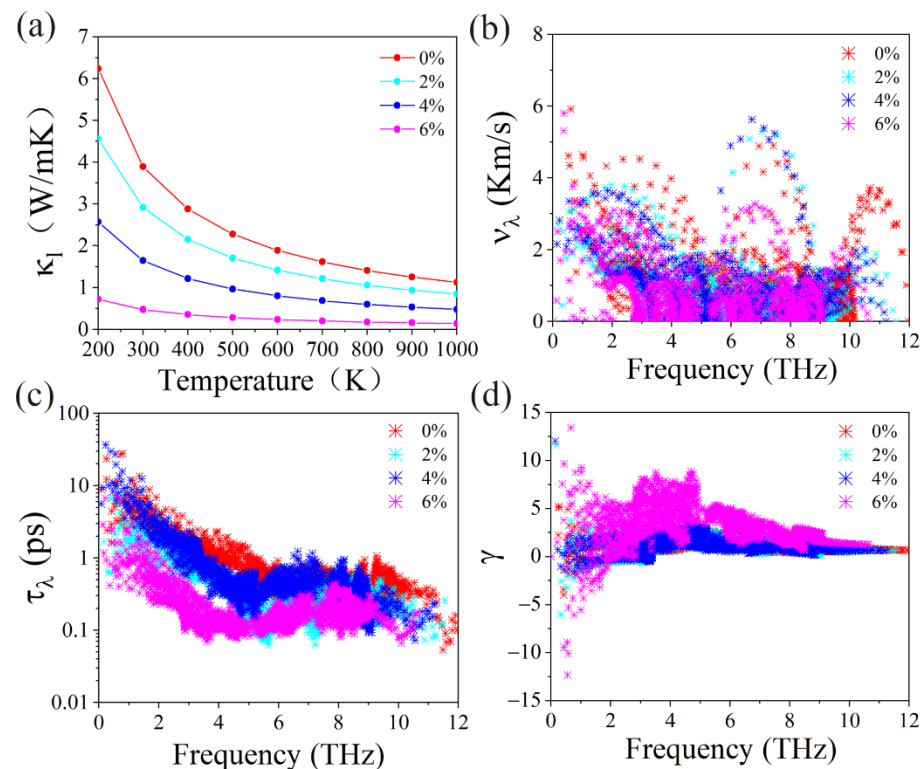

Figure 9. (**a**) The calculated lattice thermal conductivity κ_l with respect to temperature under different tensile strains for GeS$_2$ monolayer. The (**b**) phonon group velocity, (**c**) phonon relaxation time, and (**d**) Grüneisen constants for GeS$_2$ monolayer at different tensile strains.

3.4. Thermoelectric Performance

Due to the relaxation time approximation in Boltzmann transport theory, we calculated the electron relaxation time before evaluating the quality factor ZT of the GeS$_2$ monolayer. The carrier relaxation time can be defined as:

$$\tau = \frac{\mu m*}{e} \tag{3}$$

where the μ is carrier mobility, which can be estimated through deformation potential theory [55,56]:

$$\mu = \frac{2e\hbar^3 C_{2D}}{3k_B T |m*|^2 E_i^2} \tag{4}$$

where e, $\hbar$, k_B, T, and $m*$ stand for the electron charge, reduced Planck constant, Boltzmann constant, temperature, and electron (hole) effective mass, respectively. The effective mass can be defined by: $m* = \hbar^2/(\partial^2 E/\partial k^2)$, where $\hbar$ is the reduced Planck constant and E is the energy of the electron (hole) at wavevector k in the band. Therefore, the electron effective mass can be obtained from the second-order derivatives of the energy band near the conduction band minimum, while the hole's effective mass is obtained from the energy

band near the valence band maximum, and the corresponding fitting parameters are shown in Table S1. C_{2D} and E_i are the elastic modulus and deformation potential constant for 2D systems, respectively. Here, $C_{2D} = 2(\partial^2(E - E_0)/\partial\varepsilon^2)/S$, where S is the cross-sectional area. Herein, the orthorhombic lattice of the GeS$_2$ monolayer was built for the carrier mobility calculation, as plotted in Figure 10a. The band structure, total energy, and E_{edge} vs. strain for GeS$_2$ monolayer in the orthorhombic unit cell are illustrated in Figure 10b–d, respectively. The corresponding parameters calculated and mentioned above are summarized in Table 1.
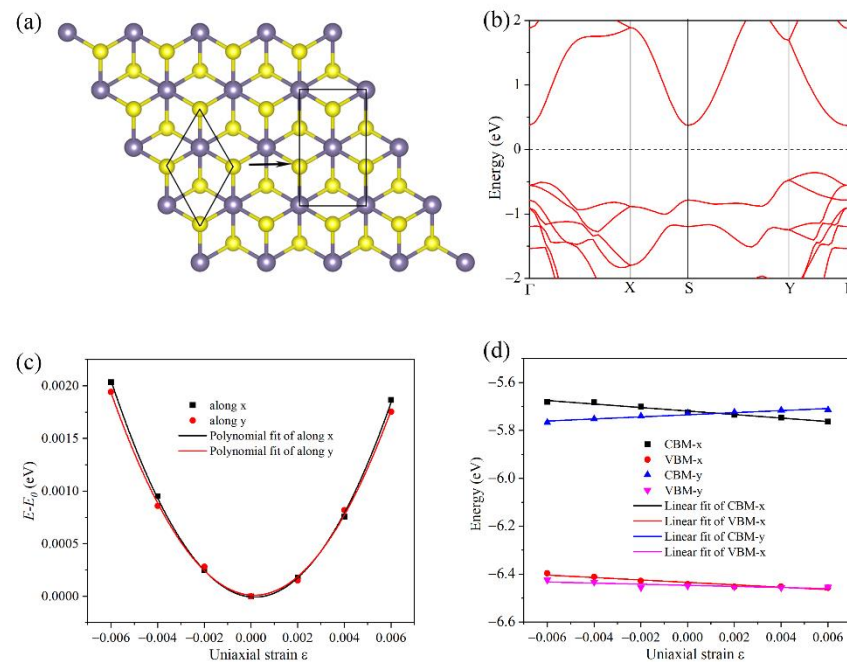

Figure 10. (**a**) The orthorhombic lattice of GeS$_2$ monolayer. The calculated (**b**) electronic band structure, (**c**) total energy shift, and (**d**) band alignment for orthorhombic lattice GeS$_2$ monolayer with respect to the uniaxial strain ε by PBE functional.

Table 1. Calculated deformation potentials (E_1), effective mass (m^*), elastic modulid (C_{2D}), carrier mobility (μ), and electronic relaxation time (τ) of GeS$_2$ monolayer under different directions.

Direction	Carrier Type	E_1 (eV)	C_{2D} (N m^{-1})	m^*/m_0	μ (cm^2 V^{-1} s^{-1})	τ (ps)
x	e	7.310	52.9	0.21	321.52	0.04
	h	5.065	52.9	0.88	37.41	0.02
y	e	4.359	49.9	0.68	79.80	0.03
	h	2.302	49.9	1.19	93.43	0.07

Finally, based on the thermoelectric parameters we obtained, the figure of merit ZT of the GeS$_2$ monolayer under different tensile strains is plotted in Figure 11. Additionally, the figure of merit ZT as a function of carrier concentrations is also shown in Figure S5. Clearly, the tensile strain greatly enhances the ZT value of the GeS$_2$ monolayer. The optimal ZT value at 300 K is 0.74 under a 6% strain, which is twice the strain-free GeS$_2$ monolayer (ZT = 0.37). This phenomenon is mainly because the tensile strain enhances the PF while reducing both κ_l and κ_e. More importantly, the ZT value will be increased from 0.74 to 0.92 with temperature increases from 300 to 700K. This value is comparable with the SiP$_2$ monolayer (0.9 at 700 K) [57], TiS$_2$ monolayer (0.95 at 300 K and an 8% tensile strain) [58], and WSSe monolayer (1.08 at 1500K and a 6% compressive strain) [48].
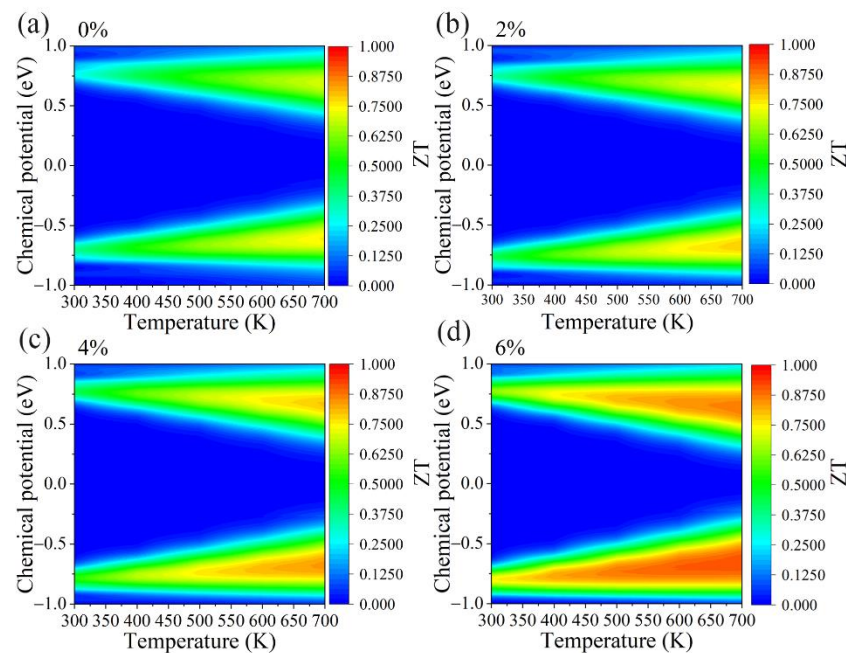
Figure 11. The contour map of the figure of merit ZT with respect to chemical potential under different biaxial tensile strains of (**a**) 0%, (**b**) 2%, (**c**) 4% and (**d**) 6% for GeS$_2$ monolayer.

4. Conclusions

In summary, by employing DFT calculations combined with semi-classical Boltzmann transport theory, the influence of tensile strain on the thermoelectric properties of the GeS$_2$ monolayer was theoretically studied. Our findings manifest that the GeS$_2$ monolayer exhibits indirect band gap semiconductor characteristics, and the band gap gradually increases with tensile strain. Moreover, the electronic and thermal transport properties of the GeS$_2$ monolayer can be efficiently tuned by tensile strain. The tensile strain can significantly enhance the power factor while decreasing thermal conductivity, leading to the enhancement of the ZT value of the GeS$_2$ monolayer. The lattice thermal conductivity of the GeS$_2$ monolayer at 300 K is only 0.48 W/mK under 6% tensile strain. This phenomenon is mainly attributed to the ultralow phonon group velocities and phonon relaxation times of GeS$_2$ monolayer under 6% strain. More importantly, the optimal ZT value of the 6% strained GeS$_2$ monolayer at room temperature is about twice more significant than the case without strain. Our results give a new insight into the strain-modulated thermoelectric performance of the GeS$_2$ monolayer.

Author Contributions: Conceptualization, R.X. and B.S.; methodology, R.X. and B.-T.W.; software, B.-T.W. and B.S.; validation, R.X., Z.C. and C.W., J.-J.M.; formal analysis, X.R. and R.X.; investigation, X.R. and R.X.; resources, B.-T.W. and B.S.; data curation, X.R. and R.X.; writing—original draft preparation, X.R. and R.X.; writing—review and editing, C.W., B.-T.W. and B.S.; visualization, R.X., Z.C., J.-J.M.; supervision, B.S.; project administration, B.S.; funding acquisition, B.-T.W. and B.S. All authors have read and agreed to the published version of the manuscript.

Institutional Review Board Statement: Not applicable.

Informed Consent Statement: Not applicable.

Data Availability Statement: The data presented in this study are available on request from the corresponding authors.

Conflicts of Interest: The authors declare no conflict of interest.

References

1. Bell, L.E. Cooling, heating, generating power, and recovering waste heat with thermoelectric systems. *Science* **2008**, *321*, 1457–1461. [CrossRef] [PubMed]
2. He, J.; Tritt Terry, M. Advances in thermoelectric materials research: Looking back and moving forward. *Science* **2017**, *357*, eaak9997. [CrossRef]
3. Mbaye, M.T.; Pradhan, S.K.; Bahoura, M. Data-driven thermoelectric modeling: Current challenges and prospects. *J. Appl. Phys.* **2021**, *130*, 190902. [CrossRef]
4. Yang, J.; Xi, L.; Qiu, W.; Wu, L.; Shi, X.; Chen, L.; Yang, J.; Zhang, W.; Uher, C.; Singh, D.J. On the tuning of electrical and thermal transport in thermoelectrics: An integrated theory—Experiment perspective. *Npj Comput. Mater.* **2016**, *2*, 15015. [CrossRef]
5. Xiong, R.; Sa, B.; Miao, N.; Li, Y.-L.; Zhou, J.; Pan, Y.; Wen, C.; Wu, B.; Sun, Z. Structural stability and thermoelectric property optimization of Ca_2Si. *RSC Adv.* **2017**, *7*, 8936–8943. [CrossRef]
6. Zhu, X.-L.; Yang, H.; Zhou, W.-X.; Wang, B.; Xu, N.; Xie, G. KAgX (X = S, Se): High-performance layered thermoelectric materials for medium-temperature applications. *ACS Appl. Mater. Inter.* **2020**, *12*, 36102–36109. [CrossRef] [PubMed]
7. Gutiérrez Moreno, J.J.; Cao, J.; Fronzi, M.; Assadi, M.H.N. A review of recent progress in thermoelectric materials through computational methods. *Mater. Renew. Sustain. Energy* **2020**, *9*, 16. [CrossRef]
8. Li, D.; Gong, Y.; Chen, Y.; Lin, J.; Khan, Q.; Zhang, Y.; Li, Y.; Zhang, H.; Xie, H. Recent progress of two-dimensional thermoelectric materials. *Nanomicro Lett.* **2020**, *12*, 36. [CrossRef] [PubMed]
9. Gan, Y.; Wang, G.; Zhou, J.; Sun, Z. Prediction of thermoelectric performance for layered IV-V-VI semiconductors by high-throughput ab initio calculations and machine learning. *Npj Comput. Mater.* **2021**, *7*, 176. [CrossRef]
10. Li, Z.; Miao, N.; Zhou, J.; Sun, Z.; Liu, Z.; Xu, H. High thermoelectric performance of few-quintuple Sb_2Te_3 nanofilms. *Nano Energy* **2018**, *43*, 285–290. [CrossRef]
11. Zhu, X.L.; Liu, P.F.; Zhang, J.; Zhang, P.; Zhou, W.X.; Xie, G.; Wang, B.T. Monolayer SnP_3: An excellent p-type thermoelectric material. *Nanoscale* **2019**, *11*, 19923–19932. [CrossRef]
12. Xie, Q.-Y.; Liu, P.-F.; Ma, J.-J.; Kuang, F.-G.; Zhang, K.-W.; Wang, B.-T. Monolayer SnI_2: An excellent p-type thermoelectric material with ultralow lattice thermal conductivity. *Materials* **2022**, *15*, 3147. [CrossRef] [PubMed]
13. Kaur, K.; Khandy, S.A.; Dhiman, S.; Sharopov, U.B.; Singh, J. Computational prediction of thermoelectric properties of 2D materials. *Electron. Struct.* **2022**, *4*, 023001. [CrossRef]
14. Sevinçli, H.; Cuniberti, G. Enhanced thermoelectric figure of merit in edge-disordered zigzag graphene nanoribbons. *Phys. Rev. B* **2010**, *81*, 113401. [CrossRef]
15. Xu, X.; Gabor, N.M.; Alden, J.S.; van der Zande, A.M.; McEuen, P.L. Photo-thermoelectric effect at a graphene interface junction. *Nano Lett.* **2010**, *10*, 562–566. [CrossRef]
16. Zhang, J.; Liu, H.J.; Cheng, L.; Wei, J.; Liang, J.H.; Fan, D.D.; Jiang, P.H.; Sun, L.; Shi, J. High thermoelectric performance can be achieved in black phosphorus. *J. Mater. Chem. C* **2016**, *4*, 991–998. [CrossRef]
17. Saito, Y.; Iizuka, T.; Koretsune, T.; Arita, R.; Shimizu, S.; Iwasa, Y. Gate-Tuned Thermoelectric Power in Black Phosphorus. *Nano Lett.* **2016**, *16*, 4819–4824. [CrossRef] [PubMed]
18. Fei, R.; Faghaninia, A.; Soklaski, R.; Yan, J.-A.; Lo, C.; Yang, L. Enhanced thermoelectric efficiency via orthogonal electrical and thermal conductances in phosphorene. *Nano Lett.* **2014**, *14*, 6393–6399. [CrossRef]
19. Chen, Z.-G.; Shi, X.; Zhao, L.-D.; Zou, J. High-performance SnSe thermoelectric materials: Progress and future challenge. *Prog. Mater. Sci.* **2018**, *97*, 283–346. [CrossRef]
20. Xu, P.; Fu, T.; Xin, J.; Liu, Y.; Ying, P.; Zhao, X.; Pan, H.; Zhu, T. Anisotropic thermoelectric properties of layered compound $SnSe_2$. *Sci. Bull.* **2017**, *62*, 1663–1668. [CrossRef]
21. Sarikurt, S.; Kocabaş, T.; Sevik, C. High-throughput computational screening of 2D materials for thermoelectrics. *J. Mater. Chem. A* **2020**, *8*, 19674–19683. [CrossRef]
22. Zhang, G.; Zhang, Y.-W. Thermoelectric properties of two-dimensional transition metal dichalcogenides. *J. Mater. Chem. C* **2017**, *5*, 7684–7698. [CrossRef]

23. Hong, J.; Lee, C.; Park, J.-S.; Shim, J.H. Control of valley degeneracy in MoS_2 by layer thickness and electric field and its effect on thermoelectric properties. *Phys. Rev. B* **2016**, *93*, 035445. [CrossRef]

24. Wickramaratne, D.; Zahid, F.; Lake, R.K. Electronic and thermoelectric properties of few-layer transition metal dichalcogenides. *J. Chem. Phys.* **2014**, *140*, 124710. [CrossRef]

25. Wang, X.; Feng, W.; Shen, C.; Sun, Z.; Qi, H.; Yang, M.; Liu, Y.; Wu, Y.; Wu, X. The verification of thermoelectric performance obtained by high-throughput calculations: The case of GeS_2 monolayer from first-principles calculations. *Front. Mater.* **2021**, *8*, 709757. [CrossRef]

26. Sa, B.; Li, Y.-L.; Qi, J.; Ahuja, R.; Sun, Z. Strain engineering for phosphorene: The potential application as a photocatalyst. *J. Phys. Chem. C* **2014**, *118*, 26560–26568. [CrossRef]

27. Yang, S.; Chen, Y.; Jiang, C. Strain engineering of two-dimensional materials: Methods, properties, and applications. *InfoMat* **2021**, *3*, 397–420. [CrossRef]

28. Du, J.; Yu, H.; Liu, B.; Hong, M.; Liao, Q.; Zhang, Z.; Zhang, Y. Strain engineering in 2D material-based flexible optoelectronics. *Small Methods* **2021**, *5*, 2000919. [CrossRef]

29. Panneerselvam, I.R.; Kim, M.H.; Baldo, C.; Wang, Y.; Sahasranaman, M. Strain engineering of polar optical phonon scattering mechanism—An effective way to optimize the power-factor and lattice thermal conductivity of ScN. *Phys. Chem. Chem. Phys.* **2021**, *23*, 23288–23302. [CrossRef] [PubMed]

30. Lou, X.; Li, S.; Chen, X.; Zhang, Q.; Deng, H.; Zhang, J.; Li, D.; Zhang, X.; Zhang, Y.; Zeng, H.; et al. Lattice strain leads to high thermoelectric performance in polycrystalline SnSe. *ACS Nano* **2021**, *15*, 8204–8215. [CrossRef]

31. Yu, C.; Zhang, G.; Zhang, Y.-W.; Peng, L.-M. Strain engineering on the thermal conductivity and heat flux of thermoelectric Bi_2Te_3 nanofilm. *Nano Energy* **2015**, *17*, 104–110. [CrossRef]

32. Guo, S.-D. Biaxial strain tuned thermoelectric properties in monolayer $PtSe_2$. *J. Mater. Chem. C* **2016**, *4*, 9366–9374. [CrossRef]

33. Blochl, P.E. Projector augmented-wave method. *Phys. Rev. B* **1994**, *50*, 17953–17979. [CrossRef]

34. Hafner, J. Ab-initio simulations of materials using VASP: Density-functional theory and beyond. *J. Comput. Chem.* **2008**, *29*, 2044–2078. [CrossRef] [PubMed]

35. Wang, G.; Peng, L.; Li, K.; Zhu, L.; Zhou, J.; Miao, N.; Sun, Z. ALKEMIE: An intelligent computational platform for accelerating materials discovery and design. *Comput. Mater. Sci.* **2021**, *186*, 110064. [CrossRef]

36. Perdew, J.P.; Burke, K.; Ernzerhof, M. Generalized Gradient Approximation Made Simple. *Phys. Rev. Lett.* **1996**, *77*, 3865–3868. [CrossRef] [PubMed]

37. Perdew, J.; Burke, K.; Ernzerhof, M. Perdew, burke, and ernzerhof reply. *Phys. Rev. Lett.* **1998**, *80*, 891. [CrossRef]

38. Monkhorst, H.J.; Pack, J.D. Special points for Brillouin-zone integrations. *Phys. Rev. B* **1976**, *13*, 5188–5192. [CrossRef]

39. Heyd, J.; Scuseria, G.E.; Ernzerhof, M. Hybrid functionals based on a screened Coulomb potential. *J. Chem. Phys.* **2003**, *118*, 8207–8215. [CrossRef]

40. Hoover, W.G. Canonical dynamics: Equilibrium phase-space distributions. *Phys. Rev. A* **1985**, *31*, 1695–1697. [CrossRef]

41. Nosé, S. A unified formulation of the constant temperature molecular dynamics methods. *J. Chem. Phys.* **1984**, *81*, 511–519. [CrossRef]

42. Madsen, G.K.H.; Singh, D.J. BoltzTraP. A code for calculating band-structure dependent quantities. *Comput. Phys. Commun.* **2006**, *175*, 67–71. [CrossRef]

43. Togo, A.; Oba, F.; Tanaka, I. First-principles calculations of the ferroelastic transition between rutile-type and $CaCl_2$-type SiO_2 at high pressures. *Phys. Rev. B* **2008**, *78*, 134106. [CrossRef]

44. Li, W.; Carrete, J.; Katcho, N.A.; Mingo, N. ShengBTE: A solver of the Boltzmann transport equation for phonons. *Comput. Phys. Commun.* **2014**, *185*, 1747–1758. [CrossRef]

45. Ding, W.; Hu, L.; Dai, J.; Tang, X.; Wei, R.; Sheng, Z.; Liang, C.; Shao, D.; Song, W.; Liu, Q.; et al. Highly ambient-sTable $1T-MoS_2$ and $1T-WS_2$ by hydrothermal synthesis under high magnetic fields. *ACS Nano* **2019**, *13*, 1694–1702. [CrossRef]

46. Nandi, P.; Rawat, A.; Ahammed, R.; Jena, N.; De Sarkar, A. Group-IV(A) Janus dichalcogenide monolayers and their interfaces straddle gigantic shear and in-plane piezoelectricity. *Nanoscale* **2021**, *13*, 5460–5478. [CrossRef] [PubMed]

47. Taheri, A.; Pisana, S.; Singh, C.V. Importance of quadratic dispersion in acoustic flexural phonons for thermal transport of two-dimensional materials. *Phys. Rev. B* **2021**, *103*, 235426. [CrossRef]

48. Chaurasiya, R.; Tyagi, S.; Singh, N.; Auluck, S.; Dixit, A. Enhancing thermoelectric properties of Janus WSSe monolayer by inducing strain mediated valley degeneracy. *J. Alloy. Compd.* **2021**, *855*, 157304. [CrossRef]

49. Li, Y.; Ma, K.; Fan, X.; Liu, F.; Li, J.; Xie, H. Enhancing thermoelectric properties of monolayer GeSe via strain-engineering: A first principles study. *Appl. Surf. Sci.* **2020**, *521*, 146256. [CrossRef]

50. Jonson, M.; Mahan, G.D. Mott's formula for the thermopower and the Wiedemann-Franz law. *Phys. Rev. B* **1980**, *21*, 4223–4229. [CrossRef]

51. Wei, Q.-L.; Zhu, X.-L.; Liu, P.-F.; Wu, Y.-Y.; Ma, J.-J.; Liu, Y.-B.; Li, Y.-H.; Wang, B.-T. Quadruple-layer group-IV tellurides: Low thermal conductivity and high performance two-dimensional thermoelectric materials. *Phys. Chem. Chem. Phys.* **2021**, *23*, 6388–6396. [CrossRef] [PubMed]

52. Xu, B.; Xia, Q.; Zhang, J.; Ma, S.; Wang, Y.; Xu, Q.; Li, J.; Wang, Y. High figure of merit of monolayer Sb_2Te_2Se of ultra low lattice thermal conductivity. *Comput. Mater. Sci.* **2020**, *177*, 109588. [CrossRef]

53. Song, H.-Y.; Sun, J.-J.; Li, M. Enhancement of monolayer HfSe$_2$ thermoelectric performance by strain engineering: A DFT calculation. *Chem. Phys. Lett.* **2021**, *784*, 139109. [CrossRef]
54. Zhou, W.X.; Cheng, Y.; Chen, K.Q.; Xie, G.; Wang, T.; Zhang, G. Thermal conductivity of amorphous materials. *Adv. Funct. Mater.* **2019**, *30*, 1903829. [CrossRef]
55. Cai, Y.; Zhang, G.; Zhang, Y.-W. Polarity-reversed robust carrier mobility in monolayer MoS$_2$ nanoribbons. *J. Am. Chem. Soc.* **2014**, *136*, 6269–6275. [CrossRef] [PubMed]
56. Rawat, A.; Jena, N.; Dimple; De Sarkar, A. A comprehensive study on carrier mobility and artificial photosynthetic properties in group VI B transition metal dichalcogenide monolayers. *J. Mater. Chem. A* **2018**, *6*, 8693–8704. [CrossRef]
57. Zhang, P.; Jiang, E.; Ouyang, T.; Tang, C.; He, C.; Li, J.; Zhang, C.; Zhong, J. Potential thermoelectric candidate monolayer silicon diphosphide (SiP$_2$) from a first-principles calculation. *Comput. Mater. Sci.* **2021**, *188*, 110154. [CrossRef]
58. Li, G.; Yao, K.; Gao, G. Strain-induced enhancement of thermoelectric performance of TiS$_2$ monolayer based on first-principles phonon and electron band structures. *Nanotechnology* **2018**, *29*, 015204. [CrossRef]